Band gap, effective masses, and energy level alignment of 2D and 3D halide perovskites and heterostructures using DFT-1/2

Boubacar Traore [*]
Univ Rennes, ENSCR, CNRS, ISCR – UMR 6226, F-35000 Rennes, France
and Univ Rennes, INSA Rennes, CNRS, Institut FOTON - UMR 6082, F-35000 Rennes, France

Jacky Even and Laurent Pedesseau
Univ Rennes, INSA Rennes, CNRS, Institut FOTON - UMR 6082, F-35000 Rennes, France

Mikaël Képénekian and Claudine Katan [†]
Univ Rennes, ENSCR, CNRS, ISCR – UMR 6226, F-35000 Rennes, France

(Received 15 November 2021; revised 11 January 2022; accepted 18 January 2022; published 31 January 2022)

We revisit the Slater half-occupation technique within the DFT-1/2 method to provide improved accuracy of 2D and 3D halide perovskites band gaps at a moderate computational cost. We propose an electron removal scheme from the halide states that drastically improve the predicted band gaps of 2D compounds. Concurrently, we compute the effective masses of the considered structures and show that DFT-1/2 describes them with a nice degree of accuracy when compared to available experimental data. Moreover, we assess the suitability of DFT-1/2 to compute the energy level alignments of this family of compounds. We compare the results in light of those we predict using the hybrid functional HSE06 and the many body perturbation theory within the *G0W*0 approximation. We discuss the limitations of our refined DFT-1/2 scheme, which tends to overestimate the downshift of the absolute valence energy levels of the layered perovskite systems. We anticipate that our results would be useful to initiate benchmark studies and investigate large systems such as heterostructures for which other approaches may be out of reach.

DOI: 10.1103/PhysRevMaterials.6.014604

I. INTRODUCTION

Metal halide perovskites (MHP) exhibited a giant leap in their solar cell efficiencies and optoelectronic properties over the past years [1,2]. While the highest efficiencies have so far been achieved in their 3D structures, their 2D counterparts are adding interesting features related to their structural diversity, stability, photophysical, and quantum confinement properties. Understanding the latter photophysical processes is key to futher exploit these materials to their full potential. Moreover engineering complex heterostructures of 3D and 2D MHP is one of the important experimental trend nowadays [3]. In both 2D and 3D compounds, the band gap value and its nature precondition their aptness to favorably perform as solar cells or light emitting diodes.

Indeed, band gap is an essential property of semiconductors and optoelectronic materials. It is fundamentally defined as the difference between the ionization energy I and the electron affinity A : $E_g = I - A$, where E_g is the fundamental or electronic band gap. Experimentally, it is measured via spectroscopic techniques such as photoemission spectroscopy (PES) and inverse photoemission spectroscopy (IPES) [4]. From the theoretical side, predicting band gaps is quite challenging. With regards to the condensed matter community, Kohn-Sham (KS) density functional theory (DFT) [5,6] is among the most popular computational methods to investigate the fundamental properties of materials. Within DFT, the computed band gap is obtained as the difference between the eigenvalues (ϵ) at the conduction band minimum (CBM) and the valence band maximum (VBM) using $E_g^{KS} = \epsilon_{\mathrm{CBM}} - \epsilon_{\mathrm{VBM}}$. However, it is known that the band gap is severely underestimated within DFT at the LDA (local density approximation) or GGA (generalized gradient approximation) levels of theory because of the self-interaction error in the occupied states [7] and the absence of the derivative discontinuity Δ_{xc} [8,9].

Various levels of theory have been developed to improve the band gap prediction of solids such as the many-body perturbation theory within the *GW* approximation [10,11], hybrid functionals [12–15], and approximations using meta-GGA based potentials [16,17], self-interaction error correction techniques [7], DFT+U [18,19], and DFT-1/2 [20]. Despite *GW* being formally among the most exact approximations for predicting fundamental band gaps of materials, its application to large systems (exceeding hundreds of electrons), with accurately converged results, becomes extremely cumbersome. With hybrid functionals, large systems start to be accessible but at the cost of high computational resources. Hence, efficient and computationally cost effective band gap correction schemes are highly desirable. Among those approaches is the

[*]boubacar.traore@univ-rennes1.fr
[†]claudine.katan@univ-rennes1.fr

Slater half occupation technique in the so-called DFT-1/2 method. So far, DFT-1/2 has been applied to predict the band gaps of a variety of materials ranging from classical semiconductors, metal oxides and 3D hybrid perovskites with a degree of accuracy comparable to *GW* [20–29]. Recently, Xue *et al.* proposed shLDA-1/2 (shell-LDA-1/2) to improve DFT-1/2 in the case of covalent semiconductors [30]. This resulted in the improvement of the band structure of Ge and the definition of some rules in the choice of the ratio of electron removal (e.g., $1/2e^-$ or $1/4e^-$) to predict the band gap of covalent semiconductors. The appealing feature of DFT-1/2 is its relative accuracy and efficiency coupled with a computational cost that is similar to standard LDA or GGA. It takes its root from the Slater transition state theory, which was generalized to solids through Janak's theorem [31]

$$\frac{\partial E(f_\alpha)}{\partial f_\alpha} = \epsilon(f_\alpha) \tag{1}$$

where $E(f_\alpha)$ is the total energy with respect to the occupation (f_α) for orbital α and $\epsilon(f_\alpha)$ is the eigenvalue at f_α. By integrating Eq. (1) between the state at which one electron is removed ($f_\alpha = -1$) and the neutral state ($f_\alpha = 0$), it is trivial to show that

$$E(0) - E(-1) \approx \epsilon\left(-\frac{1}{2}\right) \tag{2}$$

where the equality assumes a linear variation of the Kohn-Sham eigenvalues with the occupation [32]. Equation (2) tells that the eigenvalue at the half-ionized state is the negative of the ionization energy. This is at the heart of DFT-1/2 scheme and is best used when applied to the highest occupied molecular orbital (HOMO) or the valence band maximum (VBM) state. In general, the half-ionization is performed on the electronic orbitals that are present at the VBM or HOMO state. The latter information can be obtained from the projected density of states and/or from a symmetry analysis. In other words, one should not blindly proceed with DFT-1/2 without a prior knowledge of the band-edge electronic states. For instance, in the case of Ge, only half-ionized 4p states are considered because of their contribution to the VBM [20].

To benefit from Eq. (2) in a DFT self-consistent scheme, a self-energy (S_α; $2S_\alpha = \frac{\partial \epsilon_\alpha}{\partial f_\alpha}$) term is introduced, which can be interpreted as the energy necessary to localize the hole [20]. Integrating S_α and combining it with Eq. (2) leads to

$$\begin{aligned} -S_\alpha &= \int_0^{-1/2} \frac{\partial \epsilon_\alpha}{\partial f_\alpha} df_\alpha \approx \epsilon\left(-\frac{1}{2}\right) - \epsilon(0) \\ \Rightarrow E(-1) &\approx E(0) - \epsilon(0) + S_\alpha \end{aligned} \tag{3}$$

where the self-energy is assumed to be independent of the occupation [33]. The self-energy potential (V_S) is chosen such that

$$\begin{aligned} S_\alpha &= \int dr^3 \rho_\alpha(r) V_S(r) \approx \epsilon(0) - \epsilon\left(-\frac{1}{2}\right) \\ \textit{and} \qquad V_S(r) &\approx -V\left(-\frac{1}{2}, r\right) + V(0, r) \end{aligned} \tag{4}$$

ensuring that Eq. (2) is recovered. The self-energy potential is approximated by the difference between the all-electron potentials from the neutral single atoms ($V(0, r)$) and the corresponding half-ions ($V(-\frac{1}{2}, r)$). In practice, the potential $V_S(r)$ is not computed on a solid but on an isolated atom where the orbital α is located. In other words, the potentials $V(0, r)$ and $V(-\frac{1}{2}, r)$ obtained on the isolated atom of interest are used to compute $V_S(r)$ using the bottom expression in Eq. (4).

Adding V_S to the atoms in an infinite crystal leads to divergence as it falls off in the form of $1/r$. Therefore, it is trimmed with a step function using:

$$\begin{aligned} \Theta(r) &= \begin{cases} (1 - (\frac{r}{r_{\text{cut}}})^8)^3, & r \leqslant r_{\text{cut}} \\ 0, & r \geqslant r_{\text{cut}} \end{cases} \\ V_S(r) &\rightarrow V_S'(r) = V_S(r) \times \Theta(r). \end{aligned} \tag{5}$$

The trimming parameter or the cutoff radius r_{cut} is obtained variationally and is chosen so as to maximize the band gap. The power of 8 in Eq. (5) already provides good results but it may vary. To proceed with DFT-1/2 technique in a pseudopotential based DFT code, one has to identify *a priori* the electronic states contributing to VBM (or HOMO) and generate the pseudoptentials containing the self-energy potential V_S correction for these states at the atomic level.

In the context of hybrid halide perovskites, DFT-1/2 has already been implemented to improve the prediction of the band gap of 3D compounds, leading to a good agreement with experiment [26,29,34]. However, the DFT-1/2 pseudopotentials, which are generated for 3D perovskites present insufficient performance on 2D layered MHP (*vide infra*). Moreover, to the best of our knowledge, there has not yet been any report on the optimization of DFT-1/2 for 2D hybrid halide perovskites. Here, we revisit DFT-1/2 method for halide perovskites and propose, using symmetry considerations, an electron removal scheme on the halide states that drastically improves the band gaps of 2D compounds. At the same time, we show that the effective masses are also corrected. Finally, we propose a critical assessment on the ability of DFT-1/2 to predict absolute valence energy alignments or ionization energies in light of the results that we obtained from hybrid functional (HSE06) calculations and quasi-particle correction within the *GW* approximation.

II. COMPUTATIONAL METHODS

First-principles calculations were performed using the SIESTA [35,36] code based on a basis set of finite-range of numerical atomic orbitals. Norm-conserving Troullier-Martins pseudopotentials were used for each atomic species to account for the core electrons [37]. $1s^1$, $2s^22p^2$, $2s^22p^3$, $3s^23p^5$, $4s^24p^5$, $5s^25p^5$, and $5d^{10}6s^26p^2$ were used as valence electrons for H, C, N, Cl, Br, I, and Pb respectively. Polarized double-ζ (DZP) basis sets with an energy shift of 200 meV and a real space mesh grid energy cutoff of 400 Rydberg were used for the calculations. We used PBE and the revisited Slater half-occupation technique in the so-called DFT-1/2 [20] implementation for the band structure calculations. To proceed with DFT-1/2, we applied the $-\frac{1}{2}e^-$ correction scheme to the orbitals that form the VBM state of the relevant compounds. This means that for the concerned atoms, we generated DFT-1/2 corrected pseudopotentials following the bottom expression of Eq. (4). Again, we stress that

one needs to know the electronic states forming the VBM or HOMO state before using DFT-1/2. Apart from that, the main points of the theory are as described in the previous section. Spin-orbit coupling (SOC), in its on-site approximation [38], was taken into account in all calculations unless otherwise stated. Sufficient k-point grids were used to sample the different Brillouin zones. We computed the effective masses using the parabolic approximation around the band extrema.

For the 2D/3D heterostructure relaxation, we used the van der Waals density functional with C09 exchange [39] within the van der Waals DF2 flavor to describe the exchange-correlation term (we modified SIESTA version "master-post-4.1-251" to include DF2 flavor). This tuning was suggested to improve C09 based geometry optimization over that with the original DF1 flavor [40]. The in-plane lattice constants of the 3D part were imposed for the whole heterostructure and were not allowed to relax during the 2D/3D interface structural optimization. The c-lattice constant along z was allowed to relax along with the atomic positions. In order to mimic the structural properties of 3D bulk materials at room temperature, we used Cs as a pseudoatom instead of FA (FA^*PbI_3 [41], FA^* = FA replaced with Cs) and consider a thickness of 9 octahedra. The 2D structure is the room-temperature BA_2PbI_4 (BA = butylammonium) [42]. The whole heterostructure consists of 314 atoms and 1320 valence electrons. We computed the heterostructure band offsets using the Hartree Potential alignment method as described in Ref. [43].

For the absolute valence energy level alignment of the 3D systems, we used slabs constructed from SIESTA relaxed pseudocubic $CsPbI_3$ bulk structure derived from the room-temperature orthorhombic compound reported in Ref. [44]. The relaxed lattice constant $a = 6.297$ Å (the experimental pseudocubic lattice constant $a = 6.201$ Å).

Hybrid functional (HSE06 [15]) and $G0W0$ [11] calculations were performed using VASP [45,46] within the projector augmented wave (PAW) formalism [47,48]. The wave functions were expanded using a plane-wave basis set with an energy cut-off of 400 eV. We used $4 \times 4 \times 4$ and $4 \times 4 \times 1$ Γ-centered k grids to sample the Brillouin zones of the bulk (in HSE06 and $G0W0$) and slab (in HSE06) systems, respectively. We used the adaptively compressed exchange (ACE) operator [49] to reduce the computational cost of HSE06 calculations. We used 960 empty bands for $G0W0$ calculations and the convergence of the quasiparticle energies within the approximation was considered (*vide infra*). Spin-orbit coupling effect was included in all the calculations.

Except for the 2D/3D heterostructure and pseudocubic $CsPbI_3$ compound, the experimental crystal structures without any geometry optimization were used for all calculations. The following structures were considered with the space groups provided in parenthesis:

3D systems: MA^*PbI_3 (I4/mcm) [50] with MA^*= MA (methylammonium) replaced with Cs to avoid the issue of dynamical disorder of MA at high temperature phases [51], $MAPbI_3$ (Pnma) [52], FA^*PbI_3 (Pm-3m) [41], MA^*PbBr_3 (Pm-3m) [53], $MAPbBr_3$ (Pnma) [54], FA^*PbBr_3 (Pm-3m) [55], $CsPbI_3$ (Pnma) [56], $CsPbBr_3$ (Pnma) [57], $CsPbCl_3$ (Pm-3m) [58], $RbPbI_3$ (Pnma) [56], $MASnI_3$ (I4cm) [59], $CsSnI_3$ (Pnma) [60].

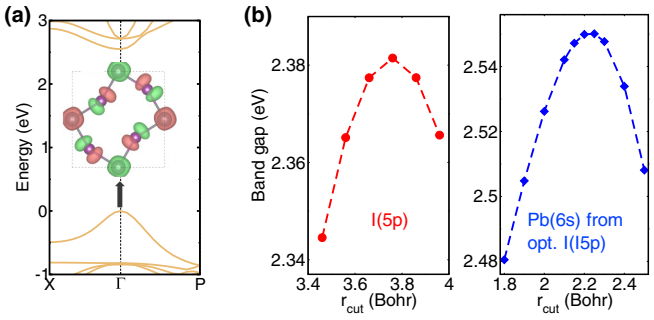

FIG. 1. Optimization of DFT-1/2 r_{cut} values of I and Pb using the tetragonal MA^*PbI_3. (a) Band structure of MA^*PbI_3 in the tetragonal phase. The wave function, without SOC, at the VBM occurring at the Γ point is also shown in the figure. (b) Optimizing r_{cut} for (left) the pseudopotential of I by removing $1/2\ e^-$ from its 5p states (right) Pb atom with the removal of $1/2e^-$ from its 6s states using the optimized I(5p) atom from the left. Here the optimal r_{cut} are ∼3.76 Bohr and ∼2.20 Bohr for I and Pb, respectively. Note that spin-orbit coupling (SOC) effect is not taken into account here since it is not necessary for the optimization of r_{cut}.

2D systems: The references of the structures used or considered are provided in Table VII. In 2D systems, the subscript n in the formula corresponds to the number of inorganic octahedra or inorganic layer thickness in the structure as, for instance, in $BA_2MA_{n-1}Pb_nI_{3n+1}$ (BA = butylammonium).

III. RESULTS AND DISCUSSION

A. DFT-1/2 for 3D metal halide perovskites

We start by applying the DFT-1/2 method to 3D halide perovskites with the general formula AMX_3 where A is a monovalent organic or inorganic cation (A = Cs, MA [MA = CH_3NH_3], FA [FA = $CH(NH_2)_2$]), X is a halide anion (X = I, Br, Cl) and M is a divalent metal cation (M = Pb, Sn...). In order to use the method, one has to know *a priori* the states contributing to the VBM of the material under study. In 3D halide perovskites, it is quite established, from first-principles calculations [61] and predicted from symmetry analysis [62] that the VBM of 3D halide perovskites is made of an antibonding hybridization between mainly X(p) and M(s) states [Fig. 1(a)]. Considering the room temperature structure of MA^*PbI_3 in the tetragonal phase (I4mcm) [50], Fig. 1 shows the optimal r_{cut} values for I and Pb that maximize the band gap of this compound [see Eq. (5)]. Comparing the DFT-1/2 band gaps (with SOC) at the optimal r_{cut} for I (1.40 eV at $r_{cut} \sim 3.76$ Bohr) and Pb (1.52 eV at $r_{cut} \sim 2.20$ Bohr + optimized r_{cut} from I) with the one obtained at the PBE+SOC level (0.35 eV), we observe that the major part of DFT-1/2 correction is due to the I(5p) states. This is consistent since the main contribution to the VBM of these compounds is due to the halide *p* states. It further supports the idea that DFT-1/2 correction on the metal cation states could generally be neglected in most semiconductors and oxides [ZnO seems to be an exception where Zn (3d) states also become important] [33]. Here, we included the correction on the metal cation (Pb and Sn) states since it brings an additional improvement as compared to experiments (*vide supra* with the

TABLE I. Cutoff radius r_{cut} (in atomic unit) and half-ionized atomic orbitals within DFT-1/2 and xs-DFT-1/2, respectively.

Atom	r_{cut} (a.u.)	Half-ionized orbital
	DFT-1/2	
Pb	2.20	6s
Sn	2.20	5s
I	3.76	5p
Br	3.44	4p
Cl	3.12	3p
	xs-DFT-1/2 for halides	
I	4.00	$5p\,(-\frac{1}{2}e^-) + 5s(-\frac{1}{4}e^-)$
Br	3.44	$4p\,(-\frac{1}{2}e^-) + 4s(-\frac{1}{4}e^-)$
Cl	3.12	$3p\,(-\frac{1}{2}e^-) + 3s(-\frac{1}{4}e^-)$
	DFT-1/2 for C, N	
C	2.40	2p
N	2.00	2p

additional 0.12 eV in MA^*PbI_3). Following the same recipe as for MA^*PbI_3, we inspected DFT-1/2 scheme with other 3D compounds including Sn, Br, and Cl and the optimal r_{cut} values are shown in Table I. Noteworthy, an optimized r_{cut} for an element in a specific compound is generally transferable to the same element in a different chemical environment using a similar r_{cut} value with only minor changes [20].

Table II summarizes DFT-1/2 corrected bands gaps for a range of 3D MHP. Previous results obtained using ppTB-mBJ potential are also included for comparison [63]. Overall, DFT-1/2 brings a substantial improvement to the band gaps of these compounds as compared to PBE. Among the investigated compounds, DFT-1/2 predicted band gaps present a mean absolute error (MAE) of 0.17 eV as compared to the experimentally reported values. When compared to ppTB-mBJ, both methods perform well with the deviation from the experiment being smaller for ppTB-mBJ (MAE of 0.11 eV).

Considering the effective masses summarized in Table III, PBE severly underestimate them by more than 50% as compared to available experimental data with a mean absolute percentage error (MAPE) of about 50%. Using ppTB-mBJ, the effective masses are improved as compared to PBE but tend to be overestimated with regards to the experimental values (MAPE $\sim$ 46.5%) as discussed thoroughly in a prior report [63]. Computed DFT-1/2 are also slightly on the high side (MAPE $\sim$ 20.2%) but with a better agreement with the available experimental data. This is consistent with previous reports that DFT-1/2 not only improves the prediction of band gaps but also the band curvatures, i.e., the effective masses [20].

B. DFT-1/2 for 2D metal halide perovskites

Here, we consider 2D MHP whose optical and photophysical properties are very often dominated by excitons [83]. Notewothy, the latter excitonic effects are not captured within DFT-1/2, which it is not intended for. We apply the 3D optimized DFT-1/2 pseudopotentials to compute the band gaps of a wide range of 2D halide perovskites. More specifically, this corresponds to removing $\frac{1}{2}e^-$ from X(p) and M(s) states. The results are summarized in Table IV. We notice that DFT-1/2 brings some improvements to the band gaps of

TABLE II. Band gap (in eV) of 3D MHP obtained with PBE, DFT-1/2 and ppTB-mBJ [63]. The space group is indicated in parenthesis. SOC effects were included in all calculations. MAE and MAPE stand for mean absolute error and mean absolute percentage error, respectively with respect to the experimental values.

3D MHP	This work PBE	This work DFT-1/2	Ref. [63] ppTB-mBJ	Exp. Exp.
MA^*PbI_3 (I4/mcm)	0.35	1.52	1.43	1.48–1.61 [64–69][a]
$MAPbI_3$ (Pnma)	0.64	1.69	1.64	1.65 [70][b]
FA^*PbI_3 (Pm-3m)	0.25	1.41		1.48[66]–1.52 [69][f]
MA^*PbBr_3 (Pm-3m)	0.52	1.97	2.16	2.18-2.22 [67,71,72][c]
$MAPbBr_3$ (Pnma)	0.88	2.29	2.43	$\sim$2.34 [73][g]
$CsPbI_3$ (Pnma)	1.91	2.79	3.33	3.17 [74][d]
FA^*PbBr_3 (Pm-3m)	0.65	2.11		$\sim$2.30 [73][g]
$CsPbBr_3$ (Pnma)	0.76	2.16	2.45	2.25 [57,75][c]
$CsPbCl_3$ (Pm-3m)	0.88	2.50	2.84	2.86 [75][c]
$RbPbI_3$ (Pnma)	1.87	2.77	3.30	3.14 [76][d]
$MASnI_3$ (I4cm)	0.22	1.27	1.55	1.2–1.4 [59][e]
$CsSnI_3$ (Pnma)	0.07	1.08	1.21	1.30 [60][c]
MAE (eV)	1.38	0.17	0.11	
MAPE (%)	68.8	7.5	5.9	

[a]Measured at 293 K or room temperature.
[b]Measured at 4.2 K.
[c]Measured at room temperature.
[d]Measured at 90 K.
[e]Measured at 200 K.
[f]High temperature tetragonal phase according to the authors (140 K – 160 K).
[g]Measured at 300 K.

TABLE III. Electron (m_e) and hole (m_h) effective masses in m_0 unit of 3D MHPs calculated with PBE, DFT-1/2, and ppTB-mBJ [63]. $\mu = m_e m_h/(m_e + m_h)$ is the reduced effective mass and $m_h = |m_v|$. For MAE and MAPE, we use the average of the computed/reported reduced effective masses for each compound.

		This work			This work			Ref.[63]			
		PBE			DFT-1/2			ppTB-mBJ			Exp.
3D MHP	Direction	m_v	m_e	μ	m_v	m_e	μ	m_v	m_e	$\boldsymbol{\mu}$	μ
MA^*PbI_3 (I4/mcm)	$\Gamma \rightarrow$ [001]	–0.07	0.07	**0.04**	–0.23	0.20	**0.11**	–0.27	0.21	**0.12**	0.104 [77] (155 K–190 K)
	$\Gamma \rightarrow$ [110]	–0.10	0.09	**0.05**	–0.26	0.26	**0.13**	–0.36	0.27	**0.15**	
	$\Gamma \rightarrow$ [111]	–0.09	0.09	**0.05**	–0.25	0.25	**0.12**	–0.33	0.25	**0.14**	
$MAPbI_3$ (Pnma)	$\Gamma \rightarrow$ [010]	–0.14	0.11	**0.06**	–0.31	0.25	**0.14**	–0.45	0.27	**0.17**	0.15 [78], 0.12 [79] (4.2 K)
	$\Gamma \rightarrow$ [101]	–0.17	0.15	**0.08**	–0.33	0.31	**0.16**	–0.50	0.34	**0.20**	
FA^*PbI_3 (Pm-3m)	R $\rightarrow$ [001]	–0.06	0.06	**0.03**	–0.22	0.21	**0.11**				0.095 [69] (140 K–160 K)
	$\Gamma \rightarrow$ [111]	–0.06	0.06	**0.03**	–0.22	0.21	**0.11**				
MA^*PbBr_3 (Pm-3m)	R $\rightarrow$ [001]	–0.10	0.11	**0.05**	–0.25	0.30	**0.14**	–0.34	0.32	**0.16**	
	$\Gamma \rightarrow$ [111]	–0.10	0.11	**0.05**	–0.25	0.29	**0.13**	–0.35	0.32	**0.17**	
$MAPbBr_3$ (Pnma)	$\Gamma \rightarrow$ [010]	–0.16	0.15	**0.08**	–0.33	0.33	**0.17**	–0.50	0.37	**0.21**	0.13 [78] (4.2 K) 0.117 [69] (2K)
	$\Gamma \rightarrow$ [101]	–0.19	0.19	**0.10**	–0.36	0.39	**0.19**	–0.59	0.44	**0.25**	
FA^*PbBr_3 (Pm-3m)	R $\rightarrow$ [001]	–0.12	0.13	**0.06**	–0.27	0.32	**0.15**				0.13 [69] (160 K–170 K)
	$\Gamma \rightarrow$ [111]	–0.12	0.13	**0.06**	–0.28	0.31	**0.15**				
$CsPbBr_3$ (Pnma)	$\Gamma \rightarrow$ [010]	–0.13	0.13	**0.07**	–0.29	0.32	**0.15**	–0.44	0.37	**0.20**	0.126 (2K) [80]
	$\Gamma \rightarrow$ [101]	–0.16	0.16	**0.08**	–0.30	0.36	**0.16**	–0.53	0.44	**0.24**	($m_h = 0.26$ [81])
$CsPbCl_3$ (Pm-3m)	R $\rightarrow$ [001]	–0.15	0.17	**0.08**	–0.29	0.40	**0.17**	–0.40	0.42	**0.20**	0.202 (2K) [82]
	$\Gamma \rightarrow$ [111]	–0.15	0.17	**0.08**	–0.29	0.40	**0.17**	–0.40	0.42	**0.20**	
MAE (m_0)			0.07			0.03			0.06		
MAPE (%)			50.1			46.5			20.2		

2D compounds as compared to PBE. However, the computed values are still largely underestimated when compared to experiment. For instance, DFT-1/2 predicts 2.20 eV for the 2D n=1 $BA_2MA_{n-1}Pb_nI_{3n+1}$, which is still 0.6 eV lower as compared to the continuum threshold from magneto-absorption experiments (2.80 eV) [84]. This becomes worse for the n = 5 compound whose computed band gap (1.36 eV) is even lower than that of the room-temperature 3D $MAPbI_3$ structure (1.52 eV from Table II). Clearly, using the 3D optimized DFT-1/2 parameters to investigate 2D perovskite structures significantly underestimates band gaps.

The inferior performance of DFT-1/2 band gap prediction for 2D MHP, considering only the correction on halide p states and Pb (6s), can to a certain extent be related to the symmetry change of VBM/CBM when going from 3D to 2D. This arises from the fundamental anisotropy of the system, and is more specifically related to the presence of apical halide atoms in 2D compounds. Indeed, from the symmetry analysis implemented for 2D halide perovskites [2,85], an additional electronic coupling appears at the VBM state: a coupling between apical X(s) and M(s) as shown in Fig. 2. This additional X(s) states expected at the VBM of 2D halide perovskites, though in a minor contribution, is absent in 3D ones. Because of the emergence of X(s) states from the symmetry analysis, we refine DFT-1/2 pseudopotentials by removing additional $\frac{1}{4}e^-$ from the s orbitals of the halide atoms. In fact, with removed $\frac{1}{2}e^-$ from X(s) orbitals, we find that the band gaps are significantly overestimated. This is not surprising since the contribution of s states to the VBM of these 2D compounds remains limited. Hereafter, DFT-1/2 with the additional $\frac{1}{4}e^-$ removed from X(s) states is referred as xs-DFT-1/2 and the corresponding r_{cut} are also reported in Table I.

At this stage, we emphasize that this adjustment (additional $\frac{1}{4}$ e-) is made in the spirit of the DFT-1/2 scheme: at its initial stage, the method may need to be readjusted to account for the chemical environment of atoms in a specific family of compounds. Noteworthy, once parameterized, the method becomes predictive *a postoriori* for similar systems where atoms exhibit similar chemical environments. For instance, we have adjusted the additional amount of electrons to be removed from X(s) within xs-DFT-1/2 on BA_2PbI_4 system only. The approach is then applied to all the other 2D systems with much improved computed band gaps as summarized Table IV.

Table IV compiles the results obtained using the refined xs-DFT/-1/2 for the considered 2D MHP. When compared to DFT-1/2, we notice a dramatic improvement in the computed band gaps using the refined method as compared to the experi-

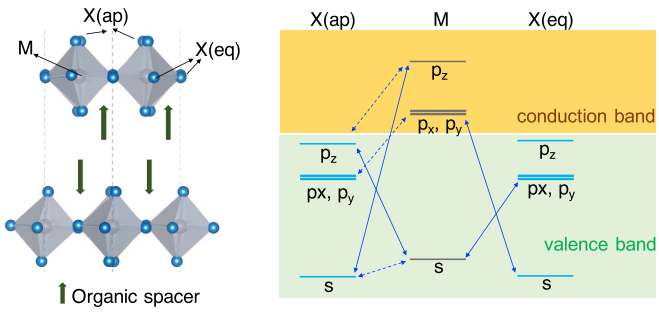

FIG. 2. Symmetry analysis of 2D MHP [2,85]. (Left) An example of a 2D MHP structure showing the apical and equatorial halide X atoms along with the central metal M atom. (Right) Electronic coupling between X and M states expected from the symmetry analysis of 2D MHP.

TABLE IV. Room temperature (otherwise specified) band gap (in eV) of 2D MHP obtained with PBE, DFT-1/2, and xs-DFT-1/2. Underlined data indicate that it was necessary to apply DFT-1/2 correction to the molecular states (containing C and N) as well. SOC effects were included in all calculations. The superscripts "*opt*" and "*el*" stand for optical and electronic band gaps, respectively. For MAE and MAPE, when the experimental electronic band gaps are not reported, we use the optical ones, which add more uncertainties to the computed statistical values.

	Layer thickness	PBE	DFT-1/2	xs-DFT-1/2	Exp.
$BA_2MA_{n-1}Pb_nI_{3n+1}$	n = 1 [42]	1.28	2.20	2.84	2.80 [84] ^{el}
	n = 2 [86]	0.87	1.82	2.45	2.44 [84] ^{el}
	n = 3 [86]	0.64	1.65	2.29	2.26 [84] ^{el}
	n = 4 [86]	0.64	1.67	2.32	2.15 [84] ^{el}
	n = 5 [87]	0.39	1.36	2.01	2.08 [84] ^{el}
$(C_mH_{2m+1}NH_3)_2PbI_4$	m = 6 [42]	1.28	2.20	2.85	2.70 [88] ^{el} (5K)
	m = 10 [89]	1.28	2.19	2.85	2.72 [90] ^{el}
$(C(NH_2)_3)(CH_3NH_3)_nPbnI_{3n+1}$	n = 1 [91]	1.12	2.05	2.70	2.27 [91] ^{opt}
	n = 2 [91]	0.72	1.67	2.31	1.99 [91] ^{opt}
	n = 3 [91]	0.16	0.87	1.46	1.73[91] ^{opt}
$PEA_2MA_{n-1}Pb_nI_{3n+1}$	n = 1 [92]	1.04	1.99	<u>2.71</u>	2.53 [93] ^{opt} (10K)
	n = 3 [94]	0.89	1.76	<u>2.34</u>	2.1 [95] ^{opt}
$(3AMP)MA_{n-1}Pb_nI_{3n+1}$	n = 1 [96]	1.02	2.02	2.69	2.23 [96] ^{opt}
	n = 2 [96]	0.39	1.27	1.83	2.02 [96] ^{opt}
	n = 3 [96]	0.30	1.23	1.82	1.92 [96] ^{opt}
$(4AMP)MA_{n-1}Pb_nI_{3n+1}$	n = 1 [96]	1.07	1.99	2.64	2.38 [96] ^{opt}
	n = 2 [96]	0.61	1.48	2.04	2.17 [96] ^{opt}
	n = 3 [96]	0.63	1.61	2.26	1.99 [96] ^{opt}
$(BA)_2(EA)_2Pb_3I_{10}$	Ref. [97]	0.99	1.94	2.54	2.12 [97] ^{opt}
$(PMA)_2PbI_4$	Ref. [98]	1.25	2.16	2.81	2.19 [99] ^{opt}
$BA_2MA_{n-1}Sn_nI_{3n+1}$	n = 1 [100]	0.82	1.83	2.37	1.83 [100] ^{opt}
	n = 3 [100]	0.12	1.07	1.59	1.50 [100] ^{opt}
$BA_2MA_{n-1}Pb_nBr_{3n+1}$	n = 1 [101]	1.61	2.70	3.37	3.34 [102] ^{el}
$PEA_2MA_{n-1}Pb_nBr_{3n+1}$	n = 1 [103]	1.72	<u>2.95</u>	3.69	2.91–2.95 [104,105] ^{opt}, 3.26 [105] ^{el}
$(BEA)_2PbBr_4$	Ref. [106]	1.78	<u>3.01</u>	3.76	
$(EA)_4Pb_3Br_{10}$	Ref. [107]	1.29	2.64	3.42	2.75 [107] ^{opt}
$(EA)_4Pb_3Cl_{10}$ [l]	Ref. [107]	1.77	3.39	4.24	3.45 [107] ^{opt}
$(PMA)_2PbCl_4$ [m]	Ref. [108]	2.30	<u>3.57</u>	<u>4.50</u>	3.65[108] ^{opt}
MAE (eV)		1.42	0.42	0.29	
MAPE (%)		61.7	18.9	12.0	

mentally reported values. This is especially true for the iodine and bromine based 2D perovskites. For instance, the continuum thresholds of the Ruddlesden-Popper (RP) phases of 2D $BA_2MA_{n-1}Pb_nI_{3n+1}$ are nicely captured by xs-DFT-1/2. For n = 4, both levels of theory lead to computed band gaps that deviate from the monotonous trend of decreasing experimental band gaps with increasing n value. This is likely due to uncertainties in the experimental crystallographic structures.

In the case of chlorine based 2D perovskites, it appears that the overestimation of the predicted band gaps is more pronounced using xs-DFT-1/2 refinement. This is possibly related to an over-correction of Cl(3p) orbital eigenvalues as a result of removing the additional $\frac{1}{4}e^-$ from its 3s states leading to larger band gaps. We note, however, that reported experimental band gaps in Table IV for chlorine compounds are optical band gaps and a fair comparison with theory should rather rely on electronic band gaps, which are lacking. This discrepancy needs more investigations on both theoretical and experimental sides. Nevertheless, xs-DFT-1/2 brings the computed band gaps closer to experiment as compared to the normal DFT-1/2.

In many of these 2D compounds, applying DFT-1/2 correction on only the inorganic states (X and M states) causes a shift of the latter states leaving behind the molecular ones. These molecular states may sometimes be spuriously located inside the band gap (underlined data in Table IV). This is an artifact of the uncorrected molecular states (Fig. 3). In those cases, it is useful to implement the DFT-1/2 method to the molecular states as well. Using the optimized r_{cut} for N and C, reported in Table I, allows to recover the correct band gaps determined by the inorganic entities (Fig. 3). This procedure may be justified by the fact that these layered systems can be conceptualized as composite materials or heterostructures where the inorganic and organic frameworks exhibit specific band alignments and their band edges may be aligned differently depending on the nature of the molecular spacers [109,110]. Incidently, even after correcting both the inorganic and organic states for $(PMA)_2PbCl_4$, some molecular states remain at the band egde implying that this compound may present a type-II band alignment as we suggested in a previous paper [110].

In Table V, we report the average of the in-plane effective masses of various 2D MHP. Similar to what has been shown

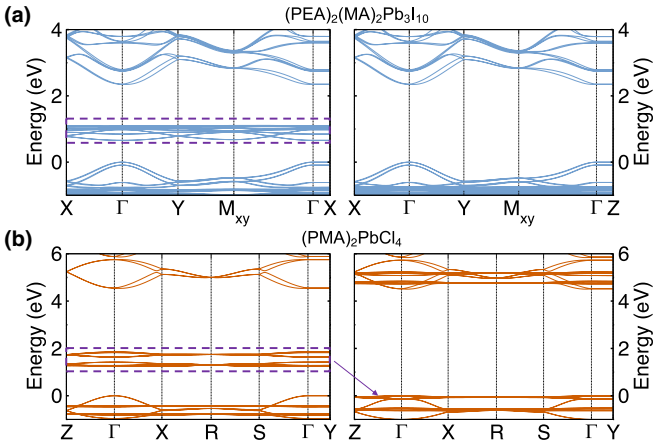

FIG. 3. Evidencing the necessity to correct molecular states in some 2D MHP. (a) Band structure of $(PEA)_2(MA)_2Pb_3I_{10}$ structure using xs-DFT-1/2 (left) without DFT-1/2 correction on molecular states and (right) with DFT-1/2 correction on molecular states. (b) Band structure of $(PMA)_2PbCl_4$ structure using xs-DFT-1/2 (left) without DFT-1/2 correction on molecular states and (right) with DFT-1/2 correction on molecular states. The molecular states are shown in the dashed rectangular boxes.

for 3D MHP, DFT-1/2 leads to a sizable increase in computed effective masses as compared to PBE. The additional correction on X(s) states leads to a further increase and in turn a better agreement with available experimentally reported values. This shows the importance of predicting more accurate band gaps for computing effective masses that are in better agreement with experiment.

C. Is DFT-1/2 more empirical than HSE06 for metal halide perovskites?

We note that within our xs-DFT-1/2 refinement, the total number of removed electrons [$\frac{3}{4}e^- \rightarrow \frac{1}{2}e^-$ (X(p)) + $\frac{1}{4}e^-$ (X(s))] somehow violates the fundamental formalism behind the DFT-1/2 theory [Eq. (2)]. In principle, this number should be $1/2e^-$ for a given atom. However, the refinement is in part justified by the fact that the method remains semi-empirical, with necessary adjustments to take into account different symmetries and chemical environments. In fact, the developpers of DFT-1/2 alluded to this in their original paper [20]. They had to change the number of removed electrons for Si (3p) from $\frac{1}{2}e^-$ to $\frac{1}{4}e^-$ to reach a good match with its experimental band gap. This readjustment was motivated by the covalent nature of Si-Si bond. But for Ge(4p), the same column as Si,

TABLE V. Average in-plane electron (m_e) and hole (m_h) effective masses in m_0 unit of 2D MHP calculated with PBE, DFT-1/2, and xs-DFT-1/2. $\mu = m_e m_h/(m_e + m_h)$ is the reduced effective mass and $m_h = |m_v|$.

		PBE			DFT-1/2			xs-DFT-1/2			Exp.
	Layer thickness	m_v	m_e	μ	m_v	m_e	μ	m_v	m_e	μ	μ
$BA_2MA_{n-1}Pb_nI_{3n+1}$	n = 1	–0.24	0.17	**0.10**	–0.43	0.26	**0.16**	–0.46	0.31	**0.18**	0.22 [83][a]
	n = 2	–0.22	0.13	**0.08**	–0.42	0.22	**0.14**	–0.45	0.26	**0.17**	0.22 [83][a]
	n = 3	–0.14	0.12	**0.06**	–0.26	0.22	**0.12**	–0.31	0.26	**0.14**	0.20 [83][a]
	n = 4	–0.13	0.11	**0.06**	–0.26	0.21	**0.12**	–0.31	0.27	**0.14**	0.20 [83][a]
	n = 5	–0.14	0.13	**0.07**	–0.25	0.23	**0.12**	–0.29	0.27	**0.14**	0.19 [83][a]
$(C_mH_{2m+1}NH_3)_2PbI_4$	m = 6	–0.25	0.17	**0.10**	–0.45	0.26	**0.16**	–0.48	0.31	**0.19**	0.18 [88][b]
	m = 10	–0.26	0.17	**0.10**	–0.46	0.26	**0.17**	–0.49	0.31	**0.19**	
$(C(NH_2)_3)(CH_3NH_3)_nPbnI_{3n+1}$	n = 1	–0.35	0.14	**0.10**	–0.65	0.23	**0.17**	–0.64	0.25	**0.18**	
	n = 2	–0.18	0.14	**0.08**	–0.32	0.24	**0.14**	–0.36	0.29	**0.16**	
	n = 3	–0.14	0.12	**0.06**	–0.23	0.22	**0.11**	–0.28	0.26	**0.13**	
$PEA_2MA_{n-1}Pb_nI_{3n+1}$	n = 1	–0.17	0.12	**0.07**	–0.30	0.21	**0.12**	–0.38	0.25	**0.15**	
	n = 3	–0.20	0.18	**0.10**	–0.34	0.30	**0.16**	–0.37	0.35	**0.18**	
$(3AMP)MA_{n-1}Pb_nI_{3n+1}$	n = 1	–0.23	0.14	**0.09**	–0.77	0.22	**0.17**	–0.40	0.29	**0.17**	
	n = 2	–0.14	0.13	**0.07**	–0.26	0.22	**0.12**	–0.29	0.26	**0.14**	
	n = 3	–0.15	0.11	**0.06**	–0.31	0.21	**0.12**	–0.33	0.26	**0.15**	
$(4AMP)MA_{n-1}Pb_nI_{3n+1}$	n = 1	–0.54	0.19	**0.14**	–0.90	0.28	**0.21**	–0.76	0.31	**0.22**	
	n = 2	–0.21	0.16	**0.09**	–0.35	0.26	**0.15**	–0.39	0.31	**0.17**	
	n = 3	–0.17	0.15	**0.08**	–0.31	0.26	**0.14**	–0.35	0.30	**0.16**	
$(BA)_2(EA)_2Pb_3I_{10}$		–0.28	0.16	**0.10**	–0.48	0.27	**0.17**	–0.51	0.33	**0.20**	
$(PMA)_2PbI_4$		–0.29	0.17	**0.11**	–0.54	0.26	**0.18**	–0.60	0.31	**0.20**	
$BA_2MA_{n-1}Sn_nI_{3n+1}$	n = 1	–0.11	0.11	**0.05**	–0.22	0.19	**0.10**	–0.25	0.22	**0.12**	
	n = 3	–0.06	0.07	**0.03**	–0.16	0.16	**0.08**	–0.20	0.20	**0.10**	
$BA_2MA_{n-1}Pb_nBr_{3n+1}$	n = 1	–0.25	0.23	**0.12**	–0.41	0.36	**0.19**	–0.45	0.43	**0.22**	
$PEA_2MA_{n-1}Pb_nBr_{3n+1}$	n = 1	–0.31	0.26	**0.14**	–0.49	0.41	**0.22**	–0.56	0.48	**0.26**	
$(BEA)_2PbBr_4$		–0.37	0.29	**0.16**	–0.57	0.46	**0.25**	–0.63	0.54	**0.29**	
$(EA)_4Pb_3Br_{10}$		–0.42	0.28	**0.17**	–0.79	0.52	**0.31**	–0.64	0.55	**0.30**	
$(EA)_4Pb_3Cl_{10}$		–0.33	0.81	**0.23**	–0.50	1.43	**0.37**	–0.56	1.03	**0.36**	

[a]Measured at 4 K.
[b]Measured at 5 K.

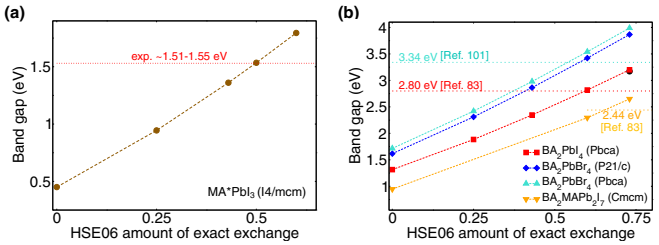

FIG. 4. Impact of the amount of HSE06 exact exchange α on band gap prediction in halide perovskites. (a) Variation of the band gap of the room temperature 3D MA^*PbI_3 MHP with the amount of exact exchange α. (b) Variation of the band gap of different 2D MHP with the amount of HSE06 exact exchange α. Horizontal dashed lines correspond to the experimentally reported electronic band gap values for the compounds of the same color.

they kept $\frac{1}{2}e^-$. More recently, DFT-1/2 was revisited for conventional semiconductors in order to obtain better quantitative estimates of band gaps leading to the so-called shell-LDA-1/2 (shLDA-1/2) [30]. In shLDA-1/2 method, some electron removal schemes (e.g., $1/2e^-$ or $1/4e^-$) and different cutoff radii for the relevant orbitals were adopted to include the effect of the chemical environment. This further illustrates the intrinsic limitation and the semi-empirical character of the method as previously discussed [111]. Anyhow, DFT-1/2 correction assumes *a priori* knowledge of the orbitals composing the VBM, by virtue of which the full *ab initio* like picture is clearly lost. It is worth noting that the strategy based on parameters tuning for band gap prediction is not unique to DFT-1/2. Meta-GGA based exchange potential in the TB-mBJ implementation also relies on parameters tuning [112]. Even the more popular hybrid functionals, such as HSE06, also include a parameter, namely the amount of the exact exchange (α). Interestingly, different amounts of exact exchange are also needed to accurately predict the band gaps of 3D and 2D MHP [113,114]. Here, we further inspect the impact of the amount of exact exchange on computed band gaps of 3D and 2D perovskites. The results are summarized in Fig. 4 and Table VI. Our results clearly show that a unique value of exact exchange α does not allow to accurately predict the band gaps of both 3D ($\alpha \sim 50\%$) and 2D ($\alpha \sim 60\%$) halide perovskite compounds. Moreover, considering the 2D MHP, one can see that the same amount of exact exchange does not perform in the same manner for iodides compounds as for bromides. Thus, the issue of accurate band gap prediction based on first-principles remains an open problem in condensed matter systems.

D. Assessing ionization energies or absolute valence energy levels using DFT-1/2

Having critically discussed the accuracy of DFT-1/2 in predicting the band gaps of halide perovskites, we further inspect the behavior of the method in predicting the absolute valence energy levels (or the ionization energies) of these compounds. We compute the absolute valence energy levels of the different systems using the Hartree potential alignment method [Fig. 5(a)] with the vacuum level set as the reference [117–119]. Indeed, by breaking the periodicity of the material along one direction (here, along z) by adding vacuum to it, forming a semi-infinite slab, allows to have the zero of the

TABLE VI. Computed band gaps of 2D and 3D halide perovskites at the HSE06 level of theory using an increasing amount of exact exchange (α). The superscripts "*opt*" and "*el*" stand for optical and electronic band gaps, respectively.

	Exact exchange α (%)	Band gap (eV)	Exp.
MA^*PbI_3 [I4/mcm] [50]	0	0.45	1.48–1.61 [64–68]
	25	0.94	
	43	1.36	
	50	1.53	
	60	1.79	
$BA_2MA_{n-1}Pb_nI_{3n+1}$ [n = 1; Pbca] [42]	0	1.31	2.80 [84] ^{el}
	25	1.88	
	43	2.34	
	60	2.82	
	73	3.20	
$BA_2MA_{n-1}Pb_nI_{3n+1}$ [n = 2; Cmcm] [86]	0	0.95	2.44 [84] ^{el}
	60	2.29	
	73	2.64	
BA_2PbBr_4 [P21/c] [101]	0	1.62	3.04–3.08 [102,115] ^{opt} 3.34 [102] ^{el}
	25	2.31	
	43	2.86	
	60	3.42	
	73	3.87	
BA_2PbBr_4 [Pbca] [116]	0	1.72	3.04–3.08 [102,115] ^{opt} 3.34 [102] ^{el}
	25	2.42	
	43	2.98	
	60	3.54	
	73	3.99	

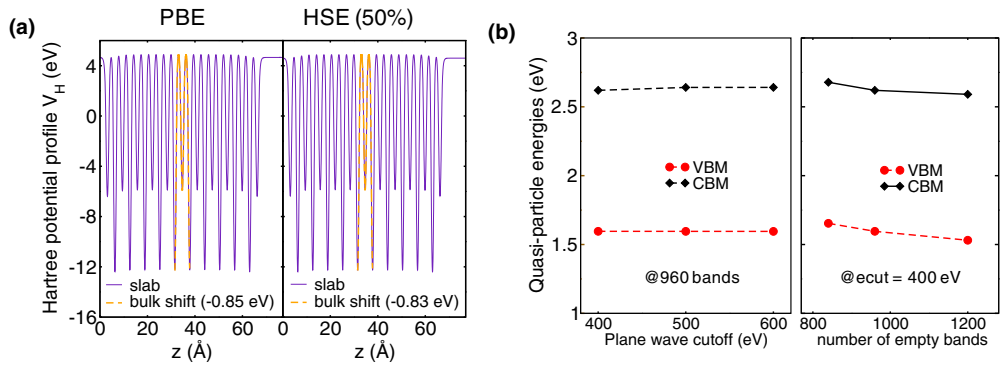

FIG. 5. Theoretical methods for the absolute energy level alignment considering $CsPbI_3$ bulk and slabs. (a) Comparison of the Hartree potential shifts computed at the PBE+SOC and HSE06+SOC ($\alpha = 50\%$) levels of theory using VASP. The figures are obtained using $CsPbI_3$ slab. ΔV_H is similar in both cases, which partly justifies the use of ΔV_H from the DFT level for the absolute valence energy level alignment using the quasiparticle energies from $G0W0$ approximation. (b) Convergence of the $G0W0$ quasiparticle energies at VB/CB of bulk $CsPbI_3$ with respect to the response function cutoff and the number of empty bands. Note that, by default, VASP uses 2/3 of the plane wave cutoff for the energy cutoff of the response function.

potential to be a well-defined quantity [120,121]. Here, the absolute valence energy level E_v^{abs} is obtained using:

$$E_v^{\text{abs}} = E_{\text{VBM}}^{\text{bulk}} + \Delta V_H + \Delta E_{\text{vacuum}} \tag{6}$$

where $E_{\text{VBM}}^{\text{bulk}}$ is the eigenvalue of the valence band maximum of the bulk system, $\Delta V_H = V_H^{\text{slab}} - V_H^{\text{bulk}}$ is the shift of the Hartree potential between the slab and the bulk systems, and $\Delta E_{\text{vacuum}} = 0 - E_{\text{vacuum}}$ is the vacuum level shift with respect to zero energy level. When considering the quasiparticle correction within the single-shot $G0W0$ approximation, we use

$$E_v^{\text{abs}} = E_{\text{VBM}}^{\text{bulk}} + \Delta\Sigma_{\text{VBM}} + \Delta V_H + \Delta E_{\text{vacuum}} \tag{7}$$

where $\Delta\Sigma_{\text{VBM}}$ is the shift in the eigenvalue of VBM due to the self-energy quasiparticle correction within $G0W0$. Here, ΔV_H is obtained from the starting mean-field theory used for the ground state calculation (PBE or HSE06). This has a minor effect on the computed E_v^{abs} since the Hartree potential shift depends on the ground state densities, which are relatively well computed at the PBE or HSE06 level [121]. Indeed, considering $CsPbI_3$ slab, Fig. 5(a) shows that ΔV_H is comparable at the PBE and HSE06 levels, which supports the use of ΔV_H from the DFT level for the absolute valence energy level alignment with the quasiparticle energies obtained from the $G0W0$ approximation. The convergence of the quasiparticle energies at VBM and CBM from the $G0W0$ approximation are shown in Fig. 5(b). For the conduction band, we added to E_v^{abs} the theoretically computed band gap of the bulk compound within the used level of theory. This then gives

$$E_c^{\text{abs}} = E_v^{\text{abs}} + E_{g,bulk} \tag{8}$$

We use $CsPbI_3$ slabs constructed from the relaxed pseudocubic $CsPbI_3$ bulk structure as model systems. We consider two different terminations of the $CsPbI_3$ slab namely CsI and PbI_2 as shown in Fig. 6(a). CsI-termination is reported to be the most stable surface from a previous theoretical calculation [122]. Figure 6(b) summarizes the predicted absolute valence energy levels for the $CsPbI_3$ slabs at different levels of theory. In all cases, PbI_2-termination presents a deeper absolute valence energy level as compared to CsI-termination for these unrelaxed slab surfaces. This can be explained by the larger surface dipoles present at the PbI_2-terminated surface, which we have thoroughly discussed in this paper [123]. DFT-1/2 predicts E_v^{abs} values that are closer to those predicted at the $G0W0$@HSE(50%) level. Here, $G0W0$@PBE presents the least negative values followed by HSE06(50%) showing the impact of the starting point for obtaining more accurate quasiparticle excitation energies [119]. DFT-1/2 tend to predict deeper E_v^{abs} values as compared to the other levels of theory. In comparison to $G0W0$@HSE(50%), DFT-1/2 differ by 0.36 eV and 0.38 eV for CsI and PbI_2-terminated surfaces, respectively. Unfortunately, a wide range of experimental values have been reported for $CsPbI_3$ ranging from 4.68 eV for β-$CsPbI_3$ [124] to 5.2 − 5.7 eV [125–128] reaching as high as 6.22 eV [129]. This hampers a proper assessment of the level of theory based on experimental data. The disparity of experimental results stems from several origins among which are process conditions, the used substrates, surface morphologies, surface terminations, crystal purity and measurement methods [130]. Based on the relatively good agreement between DFT-1/2 and G0W0@HSE(50%) results, DFT-1/2 appears to be a promising method for computing the absolute valence energy levels. This is not really surprising since the half occupation technique at the heart of DFT-1/2 leads to the negative of the ionization energy and should thus be suitable for VBM or HOMO states [*vide supra*, Eq. (2)].

Figure 6(d) compares the absolute valence energy levels of the 2D BA_2PbI_4 [42] and BA_2PbBr_4 [116] compounds computed at both DFT-1/2 and the refined xs-DFT-1/2 levels of theory. The corresponding slab is shown in Fig. 6(c). E_v^{abs} predicted with xs-DFT-1/2 tends to be much deeper (by more than 1 eV) as compared to the normal DFT-1/2. Considering the experimental absolute valence energy level alignments reported by Silver *et al.* [102] on BA_2PbI_4 (−5.8 eV) and BA_2PbBr_4 (−6.5 eV), xs-DFT-1/2 appears to overestimate E_v^{abs}. Interestingly, the computed E_v^{abs} for the two compounds using the normal DFT-1/2 fairly agree with the reported values by Silver *et al.*, which suggests that DFT-1/2 would be more reliable in predicting band offsets and energy levels related to the valence bands [more consistent with Eq. (2) to

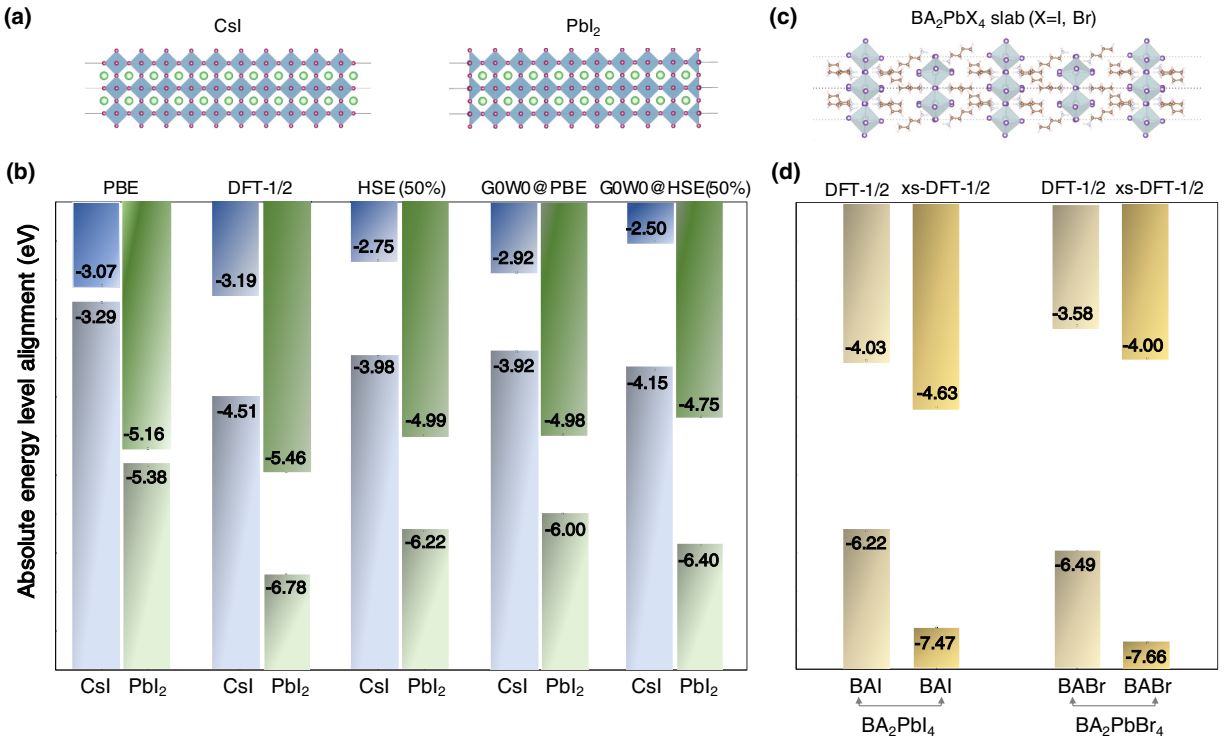

FIG. 6. Slab structures and computation of the absolute valence energy levels of MHP at different levels of theory. (a) $CsPbI_3$ slabs with CsI and PbI_2-terminations used for the computation of the absolute valence energy levels. (b) Comparison of the absolute valence energy level of pseudocubic $CsPbI_3$ with different terminations at different levels of theory. Here, PBE resuts are obtained using VASP to be consistent with HSE and $G0W0$@PBE. (c) Slab structures used to compute E_v^{abs} for BA_2PbI_4 and BA_2PbBr_4. (d) Comparison of the absolute valence energy levels of BA_2PbX_4 (X = I, Br) with BAX-termination at DFT-1/2 and xs-DFT-1/2 corrections. BAX stands for butylammonium halide (X) termination of the surface.

predict the ionization energies]. The additional $\frac{1}{4}e^-$ removed from the halide s states within xs-DFT-1/2 tends to push down the VBM states by opening the band gap but at the same time deepens the absolute valence energy level impairing the agreement with experiments. We believe that going beyond the prediction of band gaps, the refined xs-DFT-1/2 for 2D halide perovskites might present some caveats when used to infer band alignments but more investigations especially on the experimental level are needed to conclude.

E. Band alignment of a 2D/3D heterostructure

We further apply the DFT-1/2 method to compute the band alignment in a sizable halide perovskite 2D/3D heterostructure. Here, we consider the 3D FA^*PbI_3 interfaced with BA_2PbI_4 2D perovskite as explained in Sec. II [Fig. 7(a)]. Figures 7(b) and 7(c) show the computed band offsets using PBE and DFT-1/2, respectively. We predict a Type-I band alignment from both levels of theory. In particular, the 2D layer presents a barrier to holes collected from the 3D region. Referring to our discussion on the assessment of DFT-1/2 in predicting the ionization energies (*vide supra*), we postulate that our computed valence band offsets from the heterostructure would be more reliable than PBE and closer to experiment. Unfortunately, for such an extended system, implementation of $G0W0$ calculations are computationally prohibitive. Through this example, we highlight the computational efficiency of DFT-1/2 including spin-orbit coupling effect, which is of similar computational cost as a standard PBE calculation.

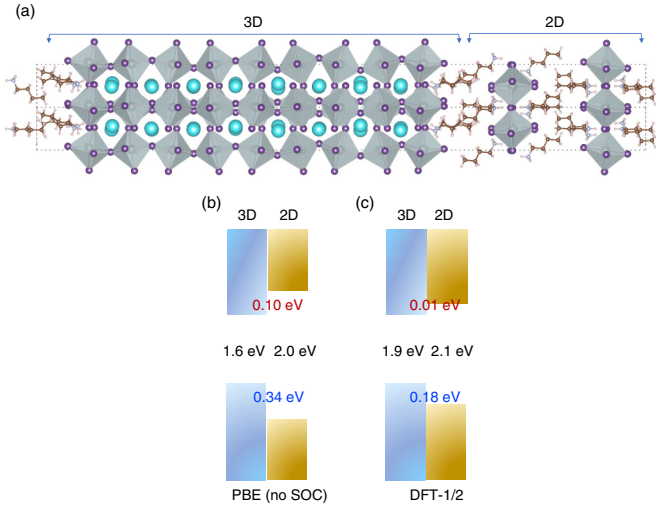

FIG. 7. Application of DFT-1/2 to compute the band alignment of a sizable 2D/3D heterostructure. (a) Constructed 2D/3D FA^*PbI_3/BA_2PbI_4 heterostructure model. In the heterostruture, both the 2D and 3D regions were terminated with BAI. (b) Computed band alignment using PBE without SOC effect. (c) Computed band alignment using DFT-1/2 including SOC effect.

TABLE VII. Comparison of the computational performance of different levels of theory using the relaxed pseudocubic $CsPbI_3$ bulk structure. Note that for PBE and DFT-1/2 calculations, inclusion of more empty bands is not necessary and has no influence on the computed eigenvalues.

	Number of bands	Number of cores	Band gap (eV)	Elapsed wall time (s)	Total computing time (s)[a]
PBE (SIESTA) [b]	160	16	0.15	52.5	840
PBE (VASP) [c]	80	16	0.22	56.4	902.4
DFT-1/2 (SIESTA)	80	16	1.32	47.1	753.6
DFT-1/2 (VASP)	80	16	1.30	65.7	1051.2
HSE06(α=50%)	192	192	1.23	1274.6	2.4×10^5
COHSEX@PBE[d]	960	960	1.36	3728.5	3.6×10^6
*G0W*0@PBE	960	960	1.02	9376.3	9.0×10^6

[a]We use: Total computing time = number of cores × elapsed wall time.
[b]SIESTA : real space mesh cutoff = 300 Ry; k-point grid = 4 × 4 × 4 point; Basis set = DZP.
[c]VASP : kinetic energy cutoff = 400 eV; k-point grid = 4 × 4 × 4.
[d]The computation of the dielectric matrix usually requires the use of a large number of empty states. Within VASP, the number of bands at the dielectric matrix step needs to be the same as in the *GW* step for computing the screened exchange self-energy Σ. Hence, our COHSEX approximation also uses a large number of bands.

F. Computational efficiency of DFT-1/2

In this section, we briefly discuss on the computational merits of DFT-1/2 as compared to more sophisticated levels of theory. This includes the hybrid functional HSE06 and the many-body perturbation theory within *G0W*0 approximation. We consider the Coulomb-hole and screened-exchange (COHSEX) approximation [131], which is the static limit of the GW approximation and appears to be more computationally efficient. We use the relaxed $CsPbI_3$ pseudocubic (a = 6.297 Å) model structure to compare the computational efficiency of the different levels of theory. Table VII summarizes the performance of *G0W*0@PBE, COHSEX@PBE, HSE06(α=50%) and DFT-1/2 to compute the band gap of the pseudocubic $CsPbI_3$ structure. Because of the static approximation to the self-energy, COHSEX presents a better computational efficiency as compared to the standard *G0W*0 calculation with a computing time that is about 2.5 times lower. However, DFT-1/2 is much more efficient as compared to either type of GW approximation or HSE06. For instance, DFT-1/2 presents a computational time that is orders of magnitude lower than that of COHSEX implementation within VASP. Besides, this COHSEX calculation requires much more memory (309.3 Mbytes), which might present an additional bottleneck for *GW* type of calculations as compared to DFT-1/2 (55.7 Mbytes using VASP). Indeed, DFT-1/2 presents a similar computational efficiency as for a standard PBE. Noteworthy, DFT-1/2 computed band gaps reach a similar accuracy as those obtained from GW calculations.

G. Conclusions

In summary, we present a generic inspection of the performance of DFT-1/2 for computing the band gaps, effective masses and band alignments of metal halide perovskites. We propose a refinement of DFT-1/2 method within the xs-DFT-1/2 approach that improves the prediction of band gaps and effective masses of 2D MHP. DFT-1/2 approach is appealing and brings orders of magnitudes improvement in the computational efficiency but at the same time produces band gaps that are comparable to those obtained from more computationally demanding state-of-the art HSE and *GW* levels of theory. The inspection of the energy level alignment further shows the capabilities of DFT-1/2 to study band alignments and predict band offsets in heterojunctions.

When compared to ppTB-mBJ, DFT-1/2 computed band gaps present a slightly larger mean absolute error as compared to experimentally reported values. However, DFT-1/2 better describe the band dispersions leading to improved effective masses as compared to ppTB-mBJ.

Regarding xs-DFT-1/2, specifically designed for layered perovskites, it improves the band gaps and effective masses as compared to normal DFT-1/2. However, beyond the computation of band gaps and effective masses, it tends to push down the VBM states by opening the band gap but at the same time deepens the predicted ionization energy values impairing the agreement with experiments. Hence, xs-DFT-1/2 might present some caveats in the context of computing band alignments but more investigations especially on the experimental level are needed to conclude.

The amount of additional electrons to be removed beyond $\frac{1}{2}e^-$ of standard DFT-1/2 is more empirical and is somehow determined through adjustments for a specific compound presenting peculiar chemical environments. Once adjusted, the method becomes predictive *a posteriori* when applied to other compounds within the same family.

Altogether, DFT-1/2 is an efficient computational method that can be useful in studying the electronic properties of large structure compounds with a good degree accuracy. Moreover, it can be interesting in large benchmark studies where comparison can be attained on sizable datasets.

ACKNOWLEDGMENTS

This work was performed with funding from the European Union's Horizon 2020 research and innovation program under Grant Agreement No. 861985 (PeroCUBE). J.E. acknowledges financial support from the Institute Universitaire de France. This work was granted access to the HPC resources of [TGCC/CINES/IDRIS] under the allocations 2020-A0100911434 and 2020-A0090907682 made by GENCI.

[1] https://www.nrel.gov/pv/cell-efficiency.html, accessed: 04-11-2021.
[2] J.-C. Blancon, J. Even, C. C. Stoumpos, M. G. Kanatzidis, and A. D. Mohite, Nat. Nanotechnol. **15**, 969 (2020).
[3] Z. Wang, Q. Lin, F. Chmiel, N. Sakai, L. Herz, and H. Snaith, Nat. Energy **2**, 17135 (2017).
[4] C. Wu, Y. Hirose, H. Sirringhaus, and A. Kahn, Chem. Phys. Lett. **272**, 43 (1997).
[5] P. Hohenberg and W. Kohn, Phys. Rev. **136**, B864 (1964).
[6] W. Kohn and L. J. Sham, Phys. Rev. **140**, A1133 (1965).
[7] T. Tsuneda and K. Hirao, J. Chem. Phys. **140**, 18A513 (2014).
[8] J. P. Perdew, R. G. Parr, M. Levy, and J. L. Balduz, Phys. Rev. Lett. **49**, 1691 (1982).
[9] J. P. Perdew, W. Yang, K. Burke, Z. Yang, E. K. U. Gross, M. Scheffler, G. E. Scuseria, T. M. Henderson, I. Y. Zhang, A. Ruzsinszky *et al.*, Proc. Natl. Acad. Sci. USA **114**, 2801 (2017).
[10] L. Hedin, Phys. Rev. **139**, A796 (1965).
[11] M. S. Hybertsen and S. G. Louie, Phys. Rev. B **34**, 5390 (1986).
[12] A. D. Becke, J. Chem. Phys. **98**, 5648 (1993).
[13] J. P. Perdew, M. Ernzerhof, and K. Burke, J. Chem. Phys. **105**, 9982 (1996).
[14] J. Heyd, G. E. Scuseria, and M. Ernzerhof, J. Chem. Phys. **118**, 8207 (2003).
[15] J. Heyd, G. E. Scuseria, and M. Ernzerhof, J. Chem. Phys. **124**, 219906 (2006).
[16] A. D. Becke and E. R. Johnson, J. Chem. Phys. **124**, 221101 (2006).
[17] F. Tran and P. Blaha, Phys. Rev. Lett. **102**, 226401 (2009).
[18] V. I. Anisimov, F. Aryasetiawan, and A. I. Lichtenstein, J. Phys.: Condens. Matter **9**, 767 (1997).
[19] S. L. Dudarev, G. A. Botton, S. Y. Savrasov, C. J. Humphreys, and A. P. Sutton, Phys. Rev. B **57**, 1505 (1998).
[20] L. G. Ferreira, M. Marques, and L. K. Teles, Phys. Rev. B **78**, 125116 (2008).
[21] M. Ribeiro, L. R. C. Fonseca, and L. G. Ferreira, Phys. Rev. B **79**, 241312(R) (2009).
[22] A. Belabbes, C. Panse, J. Furthmüller, and F. Bechstedt, Phys. Rev. B **86**, 075208 (2012).
[23] D. Q. Fang and S. L. Zhang, J. Chem. Phys. **144**, 014704 (2016).
[24] K.-H. Xue, L. R. C. Fonseca, and X.-S. Miao, RSC Adv. **7**, 21856 (2017).
[25] J.-H. Yuan, Q. Chen, L. R. C. Fonseca, M. Xu, K.-H. Xue, and X.-S. Miao, J. Phys. Commun. **2**, 105005 (2018).
[26] S. X. Tao, X. Cao, and P. A. Bobbert, Sci. Rep. **7**, 14386 (2017).
[27] M. Wu, J.-j. Shi, M. Zhang, Y.-l. Cen, W.-h. Guo, and Y.-h. Zhu, J. Mater. Chem. C **6**, 11575 (2018).
[28] R. Rodrigues Pela, A. Gulans, and C. Draxl, J. Chem. Theory Comput. **14**, 4678 (2018).
[29] D. Guedes-Sobrinho, I. Guilhon, M. Marques, and L. K. Teles, J. Phys. Chem. Lett. **10**, 4245 (2019).
[30] K.-H. Xue, Y. Junhui, L. Fonseca, and X.-S. Miao, Comp. Mater. Sci. **153**, 493 (2018).
[31] J. F. Janak, Phys. Rev. B **18**, 7165 (1978).
[32] J. R. Leite and L. G. Ferreira, Phys. Rev. A **3**, 1224 (1971).
[33] L. G. Ferreira, M. Marques, and L. K. Teles, AIP Adv. **1**, 032119 (2011).
[34] F. Valadares, I. Guilhon, L. K. Teles, and M. Marques, J. Phy. Chem. C **124**, 18390 (2020).
[35] M. Soler, E. Artacho, J. D. Gale, A. Garc, J. Junquera, P. Ordejon, and S. Daniel, J. Phys.: Condens. Matter **14**, 2745 (2002).
[36] E. Artacho, E. Anglada, O. Diéguez, J. D. Gale, A. García, J. Junquera, R. M. Martin, P. Ordejón, J. M. Pruneda, D. Sánchez-Portal, and J. M. Soler, J. Phys.: Condens. Matter **20**, 064208 (2008).
[37] N. Troullier and J. L. Martins, Phys. Rev. B **43**, 1993 (1991).
[38] L. Fernández-Seivane, M. A. Oliveira, S. Sanvito, and J. Ferrer, J. Phys.: Condens. Matter **18**, 7999 (2006).
[39] V. R. Cooper, Phys. Rev. B **81**, 161104(R) (2010).
[40] I. Hamada and M. Otani, Phys. Rev. B **82**, 153412 (2010).
[41] M. T. Weller, O. J. Weber, J. M. Frost, and A. Walsh, J. Phys. Chem. Lett. **6**, 3209 (2015).
[42] D. Billing and A. Lemmerer, Acta Crystallogr., Sect. B: Struct. Sci. **63**, 735 (2007).
[43] B. Traore, L. Pedesseau, J.-C. Blancon, S. Tretiak, A. D. Mohite, J. Even, C. Katan, and M. Kepenekian, ACS Appl. Mater. Interfaces **12**, 6633 (2020).
[44] A. Marronnier, G. Roma, S. Boyer-Richard, L. Pedesseau, J.-M. Jancu, Y. Bonnassieux, C. Katan, C. C. Stoumpos, M. G. Kanatzidis, and J. Even, ACS Nano **12**, 3477 (2018).
[45] G. Kresse and J. Furthmüller, Phys. Rev. B **54**, 11169 (1996).
[46] G. Kresse and J. Furthmüller, Comput. Mater. Sci. **6**, 15 (1996).
[47] P. E. Blöchl, Phys. Rev. B **50**, 17953 (1994).
[48] G. Kresse and D. Joubert, Phys. Rev. B **59**, 1758 (1999).
[49] L. Lin, J. Chem. Theory Comp. **12**, 2242 (2016).
[50] Y. Kawamura, H. Mashiyama, and K. Hasebe, J. Phys. Soc. Jpn. **71**, 1694 (2002).
[51] A. Poglitsch and D. Weber, J. Chem. Phys. **87**, 6373 (1987).
[52] T. Baikie, Y. Fang, J. M. Kadro, M. Schreyer, F. Wei, S. G. Mhaisalkar, M. Grätzel, and T. J. White, J. Mater. Chem. A **1**, 5628 (2013).
[53] G. A. Elbaz, D. B. Straus, O. E. Semonin, T. D. Hull, D. W. Paley, P. Kim, J. S. Owen, C. R. Kagan, and X. Roy, Nano Lett. **17**, 1727 (2017).
[54] I. Swainson, R. Hammond, C. Soullière, O. Knop, and W. Massa, J. Solid State Chem. **176**, 97 (2003).
[55] A. Franz, D. M. Többens, F. Lehmann, M. Kärgell, and S. Schorr, Acta Crystallogr., Sect. B: Struct. Sci., Cryst. Eng. Mater. **76**, 267 (2020).
[56] D. Trots and S. Myagkota, J. Phys. Chem. Solids **69**, 2520 (2008).
[57] C. C. Stoumpos, C. D. Malliakas, J. A. Peters, Z. Liu, M. Sebastian, J. Im, T. C. Chasapis, A. C. Wibowo, D. Y. Chung, A. J. Freeman *et al.*, Cryst. Growth Des. **13**, 2722 (2013).
[58] R. L. Moreira and A. Dias, J Phys. Chem Solids **68**, 1617 (2007).
[59] C. C. Stoumpos, C. D. Malliakas, and M. G. Kanatzidis, Inorg. Chem. **52**, 9019 (2013).
[60] I. Chung, J.-H. Song, J. Im, J. Androulakis, C. D. Malliakas, H. Li, A. J. Freeman, J. T. Kenney, and M. G. Kanatzidis, J Amer. Chem. Soc. **134**, 8579 (2012).
[61] J. Even, L. Pedesseau, M.-A. Dupertuis, J.-M. Jancu, and C. Katan, Phys. Rev. B **86**, 205301 (2012).
[62] J. Even, J. Phys. Chem. Lett. **6**, 2238 (2015).

[63] B. Traoré, G. Bouder, W. Lafargue-Dit-Hauret, X. Rocquefelte, C. Katan, F. Tran, and M. Kepenekian, Phys. Rev. B **99**, 035139 (2019).

[64] W. Huang, S. Yue, Y. Liu, L. Zhu, P. Jin, Q. Wu, Y. Zhang, Y. Chen, K. Liu, P. Liang *et al.*, ACS Photonics **5**, 1583 (2018).

[65] Y. Dang, Y. Liu, Y. Sun, D. Yuan, X. Liu, W. Lu, G. Liu, H. Xia, and X. Tao, CrystEngComm **17**, 665 (2015).

[66] G. E. Eperon, S. D. Stranks, C. Menelaou, M. B. Johnston, L. M. Herz, and H. J. Snaith, Energy Environ. Sci. **7**, 982 (2014).

[67] D. Shi, V. Adinolfi, R. Comin, M. Yuan, E. Alarousu, A. Buin, Y. Chen, S. Hoogland, A. Rothenberger, K. Katsiev *et al.*, Science **347**, 519 (2015).

[68] Q. Dong, Y. Fang, Y. Shao, P. Mulligan, J. Qiu, L. Cao, and J. Huang, Science **347**, 967 (2015).

[69] K. Galkowski, A. Mitioglu, A. Miyata, P. Plochocka, O. Portugall, G. E. Eperon, J. T.-W. Wang, T. Stergiopoulos, S. D. Stranks, H. J. Snaith, and R. J. Nicholas, Energy Environ. Sci. **9**, 962 (2016).

[70] C. Quarti, E. Mosconi, J. M. Ball, V. D'Innocenzo, C. Tao, S. Pathak, H. J. Snaith, A. Petrozza, and F. De Angelis, Energy Environ. Sci. **9**, 155 (2016).

[71] M. I. Saidaminov, A. L. Abdelhady, B. Murali, E. Alarousu, V. M. Burlakov, W. Peng, I. Dursun, L. Wang, Y. He, G. Maculan *et al.*, Nat. Commun. **6**, 7586 (2015).

[72] J. H. Noh, S. H. Im, J. H. Heo, T. N. Mandal, and S. I. Seok, Nano Lett. **13**, 1764 (2013).

[73] G. Mannino, I. Deretzis, E. Smecca, A. La Magna, A. Alberti, D. Ceratti, and D. Cahen, J. Phys. Chem. Lett. **11**, 2490 (2020).

[74] O. N. Yunakova, V. K. Miloslavskii, and E. N. Kovalenko, Opt. Spectrosc. **112**, 91 (2012).

[75] Z. Liu, J. A. Peters, C. C. Stoumpos, M. Sebastian, B. W. Wessels, J. Im, A. J. Freeman, and M. G. Kanatzidis, Proc. SPIE **8852**, 88520A (2013).

[76] O. N. Yunakova, V. K. Miloslavskii, E. N. Kovalenko, and E. V. Ksenofontova, Low Temp. Phys. **38**, 943 (2012).

[77] A. Miyata, A. Mitioglu, P. Plochocka, O. Portugall, J. T.-W. Wang, S. D. Stranks, H. J. Snaith, and R. J. Nicholas, Nat. Phys. **11**, 582 (2015).

[78] K. Tanaka, T. Takahashi, T. Ban, T. Kondo, K. Uchida, and N. Miura, Solid State Commun. **127**, 619 (2003).

[79] M. Hirasawa, T. Ishihara, T. Goto, K. Uchida, and N. Miura, Physica B Condens. Matter. **201**, 427 (1994).

[80] Z. Yang, A. Surrente, K. Galkowski, A. Miyata, O. Portugall, R. J. Sutton, A. A. Haghighirad, H. J. Snaith, D. K. Maude, P. Plochocka, and R. J. Nicholas, ACS Energy Lett. **2**, 1621 (2017).

[81] M. Puppin, S. Polishchuk, N. Colonna, A. Crepaldi, D. N. Dirin, O. Nazarenko, R. De Gennaro, G. Gatti, S. Roth, T. Barillot, L. Poletto, R. P. Xian, L. Rettig, M. Wolf, R. Ernstorfer, M. V. Kovalenko, N. Marzari, M. Grioni, and M. Chergui, Phys. Rev. Lett. **124**, 206402 (2020).

[82] M. Baranowski, P. Plochocka, R. Su, L. Legrand, T. Barisien, F. Bernardot, Q. Xiong, C. Testelin, and M. Chamarro, Photon. Res. **8**, A50 (2020).

[83] J.-C. Blancon, A. V. Stier, H. Tsai, W. Nie, C. C. Stoumpos, B. Traoré, L. Pedesseau, M. Kepenekian, F. Katsutani, G. T. Noe *et al.*, Nat. Commun. **9**, 2254 (2018).

[84] J.-C. Blancon, H. Tsai, W. Nie, C. C. Stoumpos, L. Pedesseau, C. Katan, M. Kepenekian, C. M. M. Soe, K. Appavoo, M. Y. Sfeir *et al.*, Science **355**, 1288 (2017).

[85] C. Quarti, C. Katan, and J. Even, J. Phys. Mater. **3**, 042001 (2020).

[86] C. C. Stoumpos, D. H. Cao, D. J. Clark, J. Young, J. M. Rondinelli, J. I. Jang, J. T. Hupp, and M. G. Kanatzidis, Chem. Mater. **28**, 2852 (2016).

[87] C. C. Stoumpos, C. M. M. Soe, H. Tsai, W. Nie, J.-C. Blancon, D. H. Cao, F. Liu, B. Traoré, C. Katan, J. Even *et al.*, Chem **2**, 427 (2017).

[88] K. Tanaka, T. Takahashi, T. Kondo, T. Umebayashi, K. Asai, and K. Ema, Phys. Rev. B **71**, 045312 (2005).

[89] A. Lemmerer and D. G. Billing, Dalton Trans. **41**, 1146 (2012).

[90] T. Ishihara, J. Takahashi, and T. Goto, Phys. Rev. B **42**, 11099 (1990).

[91] C. M. M. Soe, C. C. Stoumpos, M. Kepenekian, B. Traoré, H. Tsai, W. Nie, B. Wang, C. Katan, R. Seshadri, A. D. Mohite *et al.*, J. Am. Chem. Soc. **139**, 16297 (2017).

[92] H.-H. Fang, J. Yang, S. Adjokatse, E. Tekelenburg, M. E. Kamminga, H. Duim, J. Ye, G. R. Blake, J. Even, and M. A. Loi, Adv. Funct. Mater. **30**, 1907979 (2020).

[93] D. B. Straus, S. Hurtado Parra, N. Iotov, Q. Zhao, M. R. Gau, P. J. Carroll, J. M. Kikkawa, and C. R. Kagan, ACS Nano **14**, 3621 (2020).

[94] J. Calabrese, N. L. Jones, R. L. Harlow, N. Herron, D. L. Thorn, and Y. Wang, J. Am. Chem. Soc. **113**, 2328 (1991).

[95] M. Yuan, L. Quan, R. Comin, G. Walters, R. Sabatini, O. Voznyy, S. Hoogland, Y.-B. Zhao, E. Beauregard, P. Kanjanaboos *et al.*, Nat. Nanotechnol. **11**, 872 (2016).

[96] L. Mao, W. Ke, L. Pedesseau, Y. Wu, C. Katan, J. Even, M. R. Wasielewski, C. C. Stoumpos, and M. G. Kanatzidis, J. Am. Chem. Soc. **140**, 3775 (2018).

[97] Y. Fu, X. Jiang, X. Li, B. Traore, I. Spanopoulos, C. Katan, J. Even, M. G. Kanatzidis, and E. Harel, J. Am. Chem. Soc. **142**, 4008 (2020).

[98] G. C. Papavassiliou, G. I. Mousdis, C. P. Raptopoulou, and A. Terzis, Z. Naturforsch. **54**, 1405 (1999).

[99] C. Tian, Y. Liang, W. Chen, Y. Huang, X. Huang, F. Tian, and X. Yang, Phys. Chem. Chem. Phys. **22**, 1841 (2020).

[100] D. H. Cao, C. C. Stoumpos, T. Yokoyama, J. L. Logsdon, T.-B. Song, O. K. Farha, M. R. Wasielewski, J. T. Hupp, and M. G. Kanatzidis, ACS Energy Lett. **2**, 982 (2017).

[101] X. Gong, O. Voznyy, A. Jain, W. Liu, R. Sabatini, Z. Piontkowski, G. Walters, G. Bappi, S. Nokhrin, O. Bushuyev *et al.*, Nat. Mater. **17**, 550 (2018).

[102] S. Silver, J. Yin, H. Li, J.-L. Brédas, and A. Kahn, Adv. Energy Mater. **8**, 1703468 (2018).

[103] K. Shibuya, M. Koshimizu, F. Nishikido, H. Saito, and S. Kishimoto, Acta Crystallogr., Sect. E: Struct. Rep. Online **65**, m1323 (2009).

[104] Y. Zhang, Y. Liu, Z. Xu, H. Ye, Q. Li, M. Hu, Z. Yang, and S. F. Liu, J. Mater. Chem. C **7**, 1584 (2019).

[105] B. Guo, C. Luo, C. Yan, B. Sun, W. Li, and W. Yang, J. Phys. Chem. C **124**, 26076 (2020).

[106] D. Solis-Ibarra and H. I. Karunadasa, Angew. Chem. Int. Ed. **53**, 1039 (2014).

[107] L. Mao, Y. Wu, C. C. Stoumpos, B. Traore, C. Katan, J. Even, M. R. Wasielewski, and M. G. Kanatzidis, J. Am. Chem. Soc. **139**, 11956 (2017).
[108] W.-Q. Liao, Y. Zhang, C.-L. Hu, J.-G. Mao, H.-Y. Ye, P.-F. Li, S. D. Huang, and R.-G. Xiong, Nat. Commun. **6**, 7338 (2015).
[109] J. Even, L. Pedesseau, and C. Katan, ChemPhysChem **15**, 3733 (2014).
[110] B. Traore, L. Pedesseau, L. Assam, X. Che, J.-C. Blancon, H. Tsai, W. Nie, C. C. Stoumpos, M. G. Kanatzidis, S. Tretiak *et al.*, ACS Nano **12**, 3321 (2018).
[111] J. Doumont, F. Tran, and P. Blaha, Phys. Rev. B **99**, 115101 (2019).
[112] D. Koller, F. Tran, and P. Blaha, Phys. Rev. B **85**, 155109 (2012).
[113] M. H. Du, J. Mater. Chem. A **2**, 9091 (2014).
[114] X. Li, Y. Fu, L. Pedesseau, P. Guo, S. Cuthriell, I. Hadar, J. Even, C. Katan, C. C. Stoumpos, R. D. Schaller *et al.*, J. Am. Chem. Soc. **142**, 11486 (2020).
[115] D. Marongiu, M. Saba, F. Quochi, A. Mura, and G. Bongiovanni, J. Mater. Chem. C **7**, 12006 (2019).
[116] M. D. Smith, A. Jaffe, E. R. Dohner, A. M. Lindenberg, and H. I. Karunadasa, Chem. Sci. **8**, 4497 (2017).
[117] T. Das, X. Rocquefelte, and S. Jobic, J. Phys. Chem. C **124**, 19426 (2020).
[118] L. Lodeiro, F. Barría-Cáceres, K. Jiménez, R. Contreras, A. L. Montero-Alejo, and E. Menéndez-Proupin, ACS Omega **5**, 29477 (2020).
[119] W. Chen and A. Pasquarello, Phys. Rev. B **90**, 165133 (2014).
[120] L. Kleinman, Phys. Rev. B **24**, 7412 (1981).
[121] A. Franciosi and C. G. Van de Walle, Surf. Sci. Rep. **25**, 1 (1996).
[122] L. Long, D. Cao, J. Fei, J. Wang, Y. Zhou, Z. Jiang, Z. Jiao, and H. Shu, Chem. Phys. Lett. **734**, 136719 (2019).
[123] B. Traoré, P. Basera, A. J. Ramadan, H. J. Snaith, C. Katan, and J. Even, ACS Energy Lett. **7**, 349 (2022).
[124] Y. Wang, M. I. Dar, L. Ono, T. Zhang, M. Kan, Y. Li, L. Zhang, X. Wang, Y. Yang, X. Gao *et al.*, Science **365**, 591 (2019).
[125] Y. Hu, F. Bai, X. Liu, Q. Ji, X. Miao, T. Qiu, and S. Zhang, ACS Energy Lett. **2**, 2219 (2017).
[126] H. Bian, D. Bai, Z. Jin, K. Wang, L. Liang, H. Wang, J. Zhang, and S. L. Frank Liu, Joule **2**, 1500 (2018).
[127] K. Wang, Q. Tian, G. Zhao, J. Wen, J. Huang, C. Gao, Z. Xu, Y. Liu, L. Liang, L. Meng *et al.*, Cell Rep. Phys. Sci. **1**, 100180 (2020).
[128] J. Yuan, X. Ling, D. Yang, F. Li, S. Zhou, J. Shi, Y. Qian, J. Hu, Y. Sun, Y. Yang *et al.*, Joule **2**, 2450 (2018).
[129] S. Tao, I. Schmidt, G. Brocks, J. Jiang, I. Tranca, K. Meerholz, and S. Olthof, Nat. Commun. **10**, 2560 (2019).
[130] S. Béchu, M. Ralaiarisoa, A. Etcheberry, and P. Schulz, Adv. Energy Mater. **10**, 1904007 (2020)
[131] F. Bruneval, N. Vast, and L. Reining, Phys. Rev. B **74**, 045102 (2006)